

Scalable Learning-Based Sampling Optimization for Compressive Dynamic MRI

Submitted to *Magnetic Resonance in Medicine*

Thomas Sanchez¹, Baran Gözcü¹, Ruud B. van Heeswijk², Efe Ilıcak³,
Tolga Çukur^{3,4}, and Volkan Cevher¹

¹Laboratory for Information and Inference Systems (LIONS), EPFL, Switzerland

²Center for BioMedical Imaging (CIBM), Department of Radiology, CHUV, Switzerland

³National Magnetic Resonance Research Center (UMRAM), Bilkent University, Ankara, Turkey

⁴Department of Electrical and Electronics Engineering, Bilkent University, Ankara, Turkey

Abstract

PURPOSE: To provide a scalable and data-driven sampling mask optimization method for a given reconstruction algorithm and anatomy in the setting of dynamic MRI.

METHODS: Practical compressed sensing (CS) applications to Cartesian dynamic MRI (dMRI) have typically relied on VD random sampling masks. In contrast to this model-driven approach, the proposed method is the first data-driven, scalable framework for optimizing sampling patterns in dMRI without any model assumption. This approach allows the data to directly govern the search for a mask that exhibits good empirical performance. A previous greedy algorithm, designed for static MRI, required very intensive computations, prohibiting its direct application to dMRI; this issue is resolved by resorting to a stochastic greedy algorithm.

RESULTS: For a similar computational budget, the stochastic greedy approach yields masks which consistently improve the reconstruction accuracy for all the reconstruction algorithms, over nearly all sampling rates considered, compared to model-based approaches. Additionally, these masks do not lose any reconstruction accuracy compared to the previous greedy approach, while reducing the associated computational burden by a factor close to 60.

CONCLUSION: The numerical results suggest that data-driven driven, model-free approaches to mask design might play a preeminent role in enabling the full potential of CS applied to dMRI.

Index Terms

compressive sensing, dynamic MRI, learning-based sampling, sampling optimization

I. INTRODUCTION

One of the main challenges to the quality of dynamic Magnetic Resonance Imaging (dMRI) examinations has historically been the inefficiency of data acquisition that limits both temporal and spatial resolutions. In the presence of moving tissues, such as in cardiac MRI, the trade-off between spatial and temporal resolution is further complicated by the need to perform breath holds to minimize motion artifacts [1]. However, in the last decade, the application of Compressed Sensing (CS) to dynamic MRI (dMRI) has demonstrated a great potential to overcome some of these major limitations of dMRI.

CS allows for a successful reconstruction from undersampled measurements, provided that the data can be sparsely represented in some domain and that the measurements are incoherent [2], [3]. In dMRI, samples are acquired in the k - t space (spatial frequency and time domain), and the temporally neighboring images are highly correlated, which enables the signal to be sparsely represented in the x - f domain (image and temporal Fourier transform domain). Many algorithms have exploited this framework with great success [4]–[15]. Some other works also exploit dictionary learning, where they design a compact sparsifying transform [16]–[18], while some focus on low-rank approaches [14], [19]–[21].

While CS theory mostly focuses on fully random measurements [22], the practical implementations have generally exploited *random variable-density (VD) sampling*, proposed by Lustig et al. for static MRI [23], and applied to dMRI by Jung et al. [24]. This seminal approach draws random samples according to a parametric distribution mimicking the energy distribution of the k -space, favoring low-frequency samples. The distribution considered is typically either polynomial [13], [23], [25], [26], or Gaussian [6], [7], [14], [15], [18], [21].

The variable-density based methods commonly used in Cartesian dMRI perform well, but have several weaknesses. They require parameters to be tuned, such as decay rate of the polynomial, the standard deviation of the Gaussian distribution or the number of central phase encodes and arbitrarily constrain the sampling patterns to a model without any theoretical justification. Moreover, it is unclear which sampling density will be most effective for a given anatomy and reconstruction rule.

Recently, several publications have focused on designing alternative sampling patterns for dMRI, and we note two particularly relevant approaches. A recent state-of-the-art method devised for this purpose is the variable density incoherent spatiotemporal acquisition (VISTA) [27] that minimizes Riesz energy on a spatiotemporal grid, and has the notable advantage of generating patterns with high levels of incoherence, and maintaining uniform sampling density across frames. Another important technique proposed by Li et al. [28] develops a method for Cartesian sampling exploiting the golden-ratio, with the aim to generate incoherent measurements and maintain uniform sampling density across frames¹. Moreover, some methods exploiting training signals have been proposed for static MRI [29]–[34], but to the best of our knowledge, none of these methods have been extended to dynamic MRI.

While all these approaches allow to quickly design masks which yield a great improvement over fully random sampling, prescribed by the theory of CS, they remain fully heuristic and ignore the anatomy and the reconstruction algorithm at hand. In the present study, we propose a *scalable learning-based framework* for dMRI that, given a reconstruction algorithm, allows the data to drive the design of the sampling pattern. The present work extends the work of Gözcü et al. [35] for MRI, where they proposed a greedy method exploiting fully-sampled training data, which has the advantage of being practical, flexible, as well as theoretically grounded.

The principle behind the greedy method is the following: We start from an empty mask, compute how much adding each phase encode (horizontal line of points in Fourier space) separately to the mask increases the quality of the reconstruction over some training images with respect to a performance metric (e.g. PSNR), and pick the phase encode which maximizes it. We keep iterating on all phase encodes not yet added to the mask up to a maximal cost (e.g. 30% sampling rate). Gözcü’s approach typically uses all of the phase encodes at each iteration, which does not generalize well to dMRI due to the larger dimension of the data. The proposed stochastic greedy algorithm solves this issue by exploiting a fraction of the phases encodes at each iteration, while achieving a similar reconstruction quality, but with a *drastic runtime improvement*.

Numerical evidence shows that our framework can successfully optimize sampling masks for a broad range of decoders, from k-t FOCUSS [6] to iterative soft-thresholding [11] and ALOHA [21], outperforming state-of-the-art model-based sampling methods, relying on coherence minimization or parameter tuning, over nearly all sampling rates considered.

II. THEORY

A. Problem formulation

In the compressed sensing (CS) problem [3], one desires to retrieve a signal that is known to be sparse in some basis using only a small number of linear measurements. In the case of dynamic MRI, we consider a signal $\mathbf{x} \in \mathbb{C}^{N \times N \times T}$ (i.e. a video of size $N \times N$ with T frames), which will be written on a vectorized form $\mathbf{x} \in \mathbb{C}^p$ for convenience, and we have subsampled Fourier measurements described as

$$\mathbf{b} = \mathbf{P}_\Omega \Psi \mathbf{x} + \mathbf{w} \quad (1)$$

where $\Psi \in \mathbb{C}^p$ is the spatial Fourier transform operator applied to the vectorized signal, $\mathbf{P}_\Omega : \mathbb{C}^p \rightarrow \mathbb{C}^n$ is a subsampling operator that selects the rows of Ψ according to the indices in the set Ω with $|\Omega| = n$ and $n \ll p$. We refer to Ω as *sampling pattern* or *mask*. We assume the signal \mathbf{x} to be sparse in the basis Φ , which typically is a temporal Fourier transform across frames [6], [11]–[15], [21]. Given the samples \mathbf{b} , along with Ω , a *reconstruction algorithm* or *decoder* g forms an estimate $\hat{\mathbf{x}}$ of \mathbf{x} such that

$$\hat{\mathbf{x}} = g(\mathbf{b}, \Omega) \quad (2)$$

Many reconstructions have been proposed over the years, and we detail hereafter several state of the art methods that will be considered in Section IV for simulated undersampling experiment on single-coil datasets. An early

¹This approach is different from the commonly used *golden-angle* sampling used in radial sampling.

approach for successful CS recovery in dynamic MRI is k-t FOCUSS [6], which approximates the result of the problem

$$\min_{\mathbf{x} \in \mathbb{C}^p} \|\Phi \mathbf{x}\|_1 \text{ s.t. } \|\mathbf{P}_\Omega \Psi \mathbf{x} - \mathbf{b}\|_2 \leq \epsilon. \quad (3)$$

A later method is the Iterative Soft-Thresholding (IST), which directly solves the problem (3) [11]. More recently, a generic framework for both single and multi-coil dMRI was developed named annihilating filter based low-rank Hankel matrix approach (ALOHA) by Jin et al. [21]. ALOHA exploits the duality between sparse signals and their transform domain representations cast as a low-rank Hankel matrix. This duality can be used to reformulate the CS recovery as a low-rank matrix completion problem.

Many other algorithms have been developed to reconstruct undersampled dynamic MRI images with Cartesian sampling, and the first one to be used was k-t SPARSE [4], which solves the problem (3) with a conjugate gradient method. Other approaches combined low-rank and sparse approaches [13], [14], [19], or used dictionary learning to sparsely represent a signal [17], [18], [36], and more recently, deep learning reconstructions [15] have yielded promising results. While we primarily consider Cartesian dMRI here, non-Cartesian sampling, typically based on radial trajectories, has also been used to broadly enable free-breathing scans [12], [37].

B. Learning-based approaches to mask design

1) *Model-free approach*: Our work follows the learning-based framework of [35], and we summarize their main ideas hereafter. We assume that we have a set of training samples $\mathbf{x}_1, \dots, \mathbf{x}_m \in \mathbb{C}^{N \times N \times T}$ representative of an unknown signal of interest \mathbf{x} . This means that they are all drawn from the same unknown probability distribution P . We are concerned here by the noiseless case, i.e. $\mathbf{w} = 0$, and the noisy case is covered in Section 4 of the Supplementary Material.

We wish to find the sampling pattern Ω^* that will perform best on \mathbf{x} , according to some *performance metric* $\eta(\mathbf{x}, \hat{\mathbf{x}})$, and given some constraints on the design of the mask. A performance metric enables quantification of the similarity of a reconstructed image to the ground truth, and common metrics include Peak Signal-to-Noise Ratio (PSNR), Mean Square Error (MSE) and Structural Similarity Index Measure (SSIM) [38]. Regarding the constraints on Ω , it is desirable to restrict the sampling pattern to contain for instance only horizontal and/or vertical phase encoding directions. To formalize this, we define a set \mathcal{S} of subsets of $\{1, \dots, p\}$ which typically contains phase encoding lines in the k-space. The final mask then takes the form

$$\Omega = \bigcup_{j=1}^{\ell} S_j, \quad S_j \in \mathcal{S} \quad (4)$$

for some $\ell > 0$. We assume that there exists a *cost function* $c(\Omega) > 0$ associated with each sampling pattern, and that the final cost must satisfy $c(\Omega) \leq \Gamma$ for some $\Gamma > 0$, and we consider here the case where the cost is the total number of indices in Ω (constraint on the sampling rate). This then leads to the problem of finding the mask that maximizes

$$\Omega^* = \arg \max_{\Omega \in \mathcal{A}} \mathbb{E}_P [\eta(\mathbf{x}, \hat{\mathbf{x}})] \quad (5)$$

where \mathcal{A} is the set of feasible Ω according to \mathcal{S} , $c(\cdot)$, Γ . Due to the problem (5) not being tractable in practice, we look for an approximate maximizer in the form of the *empirical average*, which yields the selection rule that will be used in the sequel

$$\hat{\Omega} = \operatorname{argmax}_{\Omega \in \mathcal{A}} \frac{1}{m} \sum_{j=1}^m \eta(\mathbf{x}_j, \hat{\mathbf{x}}_j). \quad (6)$$

Given that enough training samples are considered, statistical learning theory guarantees that the result obtained using the empirical average will be close to the true average, and Proposition 1 of [35], which formalizes and proves this, extends to the present case as well.

2) *Greedy algorithm*: Before moving on to our stochastic greedy method, we describe the straightforward application of Gözcü's framework to dMRI. Because finding the exact maximizer of (6) is difficult in general, the greedy algorithm proposed by Gözcü et al. [35] finds an approximate solution by exploiting the fact that the generalization bound dictates that a mask with improved performance should always be favored. This greedy

approach has the advantage over state-of-the-art methods of being parameter free in the sense that no tuning is required for the mask selection process, once the reconstruction algorithm and its parameters are given.

The details are specified in Algorithm 1.a. We start from a base mask Ω , and at each iteration, we create candidate masks $\Omega' = \Omega \cup S$ with each subset $S \in \mathcal{S}$ not yet included in the mask Ω . After reconstructing the image $\hat{\mathbf{x}}$ in the training dataset using the decoder g for all the Ω' , the subset S that yields the larger increase regarding the performance metric η is permanently added to the mask Ω . The algorithm continues to add subsets from \mathcal{S} while the cost constraint Γ is not violated.

The algorithm also exhibits a useful *nestedness* property, which means that both the order in which the samples are added to the mask and their cost are known. Once a given cost is reached (e.g. 30% sampling), all the masks for smaller costs remain available (e.g. the mask for 20% sampling rate). However, there is a limited applicability of Algorithm 1.a to dMRI that comes from the fact that the number of samples increases linearly with the number of frames, and that the reconstruction algorithms are generally more expensive to run than in the static case. This makes the overall running time of Algorithm 1.a impractical for the present case, as we will see in Section IV.

Algorithm 1 Greedy mask optimization algorithms for dMRI

(1.a) refers to the **greedy** algorithm

(1.b) refers to the **Stochastic greedy** algorithm

(1.c) refers to the **Stochastic cycling greedy** algorithm

Input: Training data $\mathbf{x}_1, \dots, \mathbf{x}_m$, reconstruction rule g , sampling subset \mathcal{S} , cost function c , maximum cost Γ

Output: Sampling pattern Ω

1: (1.c) Initialize $t = 1$

2: **while** $c(\Omega) \leq \Gamma$ **do**

3: $\left\{ \begin{array}{l} \text{(1.a) Pick } \mathcal{S}_{iter} = \mathcal{S} \\ \text{(1.b) Pick } \mathcal{S}_{iter} \subseteq \mathcal{S}, \text{ at random, with } |\mathcal{S}_{iter}| = k \\ \text{(1.c) Pick } \mathcal{S}_{iter} \subseteq \mathcal{S}_t, \text{ at random, with } |\mathcal{S}_{iter}| = k \end{array} \right.$

4: **for** $S \in \mathcal{S}_{iter}$ such that $c(\Omega \cup S) \leq \Gamma$ **do**

5: $\Omega' = \Omega \cup S$

6: For each j , set $\mathbf{b}_j \leftarrow \mathbf{P}_{\Omega'} \Psi \mathbf{x}_j$, $\hat{\mathbf{x}}_j \leftarrow g(\Omega', \mathbf{b}_j)$

7: $\eta(\Omega') \leftarrow \frac{1}{m} \sum_{j=1}^m \eta(\mathbf{x}_j, \hat{\mathbf{x}}_j)$

8: $\Omega \leftarrow \Omega \cup S^*$, where

$$S^* = \underset{S: c(\Omega \cup S) \leq \Gamma}{\operatorname{argmax}} \frac{\eta(\Omega \cup S) - \eta(\Omega)}{c(\Omega \cup S) - c(\Omega)}$$

9: (1.c) $t = t \bmod T + 1$

10: **return** Ω

3) *Stochastic greedy algorithms:* To address the scalability issue of Algorithm 1.a, we consider a subset \mathcal{S}_{iter} of \mathcal{S} , chosen either at random (Algo. 1.b), or at random *from the t -th frame*, which will be denoted as $\mathcal{S}_{iter} \subseteq \mathcal{S}_t$ (Algo. 1.c). Then, the same greedy procedure as Algorithm 1.a is run, and at the end of an iteration, either a new subset of \mathcal{S} is selected at random (Algo. 1.b), or the index of the selected frame is incremented (Algo. 1.c) and a subset is drawn at random from this frame. The number of samples used at each iteration is given by the batch size k . It is important to highlight that this approach preserves all the benefits of the previous greedy approach: our method remains nearly parameter free even when considering the batch size k . Empirical results in section IV-A suggest that the tuning of this parameter is simple and does not change the accuracy of reconstruction when chosen as a reasonable fraction of the total number of phase encoding lines.

The main difference between Algorithms 1.b and 1.c lies in the way the random subset is chosen. This difference has the practical implication that the sampling masks designed in Algorithm 1.c will have the same number of samples per frame, which is desirable for a dMRI scan [27], as undersampling frames at different rates may alter the temporal resolution, thus leading to potentially missing critical temporal events.

C. Learning-based variable density

An intuitive approach given in [35] is to find an approximative solution to the combinatorial problem (6) by generating a set of candidate masks $\Omega_1, \dots, \Omega_L$ using parametric variable-density methods, and choose the one with the best empirical performance on the training set (Algorithm 2). While similar ideas have already been used when performing parameter sweeps in existing works (e.g., see [30]), the framework of [35] justifies why the empirical performance is the correct quantity to optimize.

Algorithm 2 Learning-based variable density (LB-VD)

Input: Training data $\mathbf{x}_1, \dots, \mathbf{x}_m$, reconstruction rule g , candidate masks $\Omega_1, \dots, \Omega_L$

Output: Sampling pattern Ω

- 1: **for** $\ell = 1, \dots, L$ **do**
 - 2: For each j , set $\mathbf{b}_j \leftarrow \mathbf{P}_{\Omega_\ell} \Psi \mathbf{x}_j$, $\hat{\mathbf{x}}_j \leftarrow g(\Omega_\ell, \mathbf{b}_j)$
 - 3: $\eta_\ell \leftarrow \frac{1}{m} \sum_{j=1}^m \eta(\mathbf{x}_j, \hat{\mathbf{x}}_j)$
 - 4: $\Omega \leftarrow \Omega_{\ell^*}$, where $\ell^* = \operatorname{argmax}_{\ell=1, \dots, L} \eta_\ell$
 - 5: **return** Ω
-

III. METHODS

A. Data acquisition

The first dataset was acquired on seven healthy adult volunteers with a balanced steady-state free precession (bSSFP) pulse sequence on a whole-body Siemens 3T scanner using a 34-element matrix coil array. The study was approved by the local institutional review board, and informed consent was obtained from all subjects prior to imaging. Several short-axis cine images were acquired during a breath-hold scan. Fully sampled Cartesian data were acquired using a 256×256 grid, with the following relevant imaging parameters: $320 \text{ mm} \times 320 \text{ mm}$ field of view (FoV), 6 mm slice thickness, $1.37 \text{ mm} \times 1.37 \text{ mm}$ spatial resolution, 42.38 ms temporal resolution, 1.63/3.26 ms TE/TR, 36° flip angle, 1395 Hz/px readout bandwidth. There were 13 phase encodes acquired for a frame during one heartbeat, for a total of 25 frames after the scan.

The Cartesian cardiac scans were then combined to single coil data from the initial $256 \times 256 \times 25 \times 34$ size, using adaptive coil combination [39], [40], which keeps the images complex. This single coil image was then cropped to a $152 \times 152 \times 17$ image. This is done because a large portion of the periphery of the images are static or void, and also to enable a greater computational efficiency. These scans are the ones we used as the basis of the subsequent numerical experiments.

The second dataset that we used comprised 4 vocal tract scans with a 2D HASTE sequence (T2 weighted single-shot turbo spin-echo) on a 3T Siemens Tim Trio using a 4-channel body matrix coil array. The study was approved by the local institutional review board, and informed consent was obtained from all subjects prior to imaging. Fully sampled Cartesian data were acquired using a 256×256 grid, with $256 \text{ mm} \times 256 \text{ mm}$ field of view (FoV), 5 mm slice thickness, $1 \text{ mm} \times 1 \text{ mm}$ spatial resolution, 98/1000 ms TE/TR, 150° flip angle, 391 Hz/px readout bandwidth, 5.44 ms echo spacing (256 turbo factor). There was a total of 10 frames acquired, which were recombined to single coil data using adaptive coil combination as well [39], [40].

B. Reconstruction algorithms

As detailed in the Section II-A, we consider three reconstruction algorithms, namely *k-t FOCUSS* (KTF) [6], *Iterative Soft-Thresholding* (IST) [11] and *ALOHA* [21]. Their parameters were selected to maintain a good empirical performance across all sampling rates considered.

- *KTF*: we used 2 outer iterations with 40 inner iterations, and a low-phase estimate of \mathbf{W} with 4 phase encodes and set the power in the diagonal of \mathbf{W} to $p = 0.5$, and the Lagrangian parameter of the inner problem to $\lambda = 0$.
- *IST*: the regularization parameter was set to $\lambda = 0.046$ and decreased by 1.7% at each iteration, as suggested in [11]. The maximal number of iterations was 100.
- *ALOHA*: the annihilating filter was of size 5×5 , with three levels of pyramidal decomposition with tolerances $(10^{-1}, 10^{-2}, 10^{-3})$ at each scale. The ADMM parameter was set to $\mu = 10$.

C. Sampling optimization algorithms

In addition to the greedy methods in Algorithm 1, we consider the following comparison baselines from the literature:

leftmargin=*

- *Coherence-VD* [23]: We consider a random *variable-density* sampling mask with Gaussian density and a fixed number of fully sampled low frequency phase encodes. We varied the standard deviation of the Gaussian distribution to minimize the coherence using a Monte-Carlo procedure, as suggested in [12], [23].
- *LB-VD* (Algorithm 2): We considered a random *variable-density* sampling mask with Gaussian density sampling. In this setting, we optimized the number of fully sampled low frequency phase encodes, as well as the standard deviation of the Gaussian distribution in order to maximize the performance metric on the same training set that was used for the greedy algorithm. This was achieved using a parameter sweep, and for each set of parameters, the results were averaged over 20 random masks produced by sampling from the corresponding distribution.
- *Golden-ratio Cartesian sampling* [28]: This method, referred to as *golden*, does not have free parameters. It is a nonlinear function of the golden-ratio to distribute the phase encodes across the frames. Note again that this is a very different approach from the state-of-the-art golden angle sampling used in radial MRI.

For the greedy methods in Algorithms 1.a, 1.b, and 1.c, we typically considered the sampling subset \mathcal{S} to be the set of phase encode lines across all frames (i.e. for an image of size $152 \times 152 \times 17$, the full set contains $|\mathcal{S}| = 152 \times 17 = 2584$ sets of subsets). Then, the cost function c was taken as the sampling rate of the mask, and Γ was 15% sampling. The performance metric η was taken as either PSNR or SSIM.

All of the computations were carried out using MATLAB 2017a (MathWorks, Natick). The computations for the greedy algorithms and LB-VD were run on a computing cluster using MATLAB's Parallel Computing Toolbox.

D. Computational complexity

Greedy algorithms 1.a and 1.c: The reconstruction times for the different settings (image sizes, number of training samples) are displayed in the Table I. Algorithm 1.b is not included in this analysis, because it has the same computational complexity as 1.c. First of all, note that the overall runtime heavily depends on the reconstruction algorithm in use, and varies from 1.2s for IST and 3.5s for KTF to 73.5s for ALOHA; however this does not take into account the *significant* latency introduced by running the simulation in parallel. Due to the very small number of samples used by the stochastic algorithm, the running time improvement over the standard greedy algorithm is tremendous. We will see in Section IV-A that there is *nearly no performance loss* linked to this acceleration.

It is also important to highlight that these computations are carried out *offline*, and have to be done only once for a fixed anatomy and resolution, while giving access to the masks up to the highest sampling rate achieved (typically 30% in the present case) due to the nestedness property of the greedy algorithm. Given the improvements to both the running time and the scalability compared to the previous version of the greedy algorithm, as well as the result of yielding a mask tailored for a certain anatomy, the computational times of the stochastic cycling greedy algorithm in Table I should not be seen as a critical issue.

Learning-based variable-density Gaussian sampling (LB-VD - Algorithm 2): In this setting, we optimize the parametric Gaussian distribution for PSNR and we summarize the parameters that we examined in Table II. The parameters that we considered are the standard deviation of the distribution, as well as the size of the fully sampled low-frequency region. For each set of parameters and training samples, the results were averaged across 20 draws. The number of reconstructions is similar to the ones performed by the stochastic greedy algorithms, but the running time is much shorter. This is due to the fact that this problem can be distributed more efficiently and requires much less communication between workers than the greedy algorithms. This model-based method will be compared with the greedy methods in the sequel.

A first limitation appears in the fact that while the LB-VD mask optimization requires roughly the same number of reconstructions as the stochastic greedy methods, it only provides masks for a discrete set of sampling rates (in our comparisons, we used 12 sampling rates from 2.5% to 30%, with 2.5% intervals). However, the greedy method enables mask optimization for a continuous range of sampling rates by exploiting the information from other sampling rates to further guide the mask design which is not the case for LB-VD.

Table I: Running time of the greedy algorithms for different decoders and training data sizes. The setting corresponds to $n_x, n_y, n_{frames}, n_{train}$. n_{procs} is the number of parallel processes used by each simulation. * means that the runtime was extrapolated from a few iterations.

Algorithm	Setting	Greedy			Stochastic cycling greedy			Speedup
		n_{recon}	n_{procs}	Time	n_{recon}	n_{procs}	Time	
KTF	$152 \times 152 \times 17 \times 3$	$5.1 \cdot 10^6$	152	6d 23h	$8.8 \cdot 10^4$	38	11h 40	58
	$256 \times 256 \times 10 \times 2$	$3.3 \cdot 10^6$	256	$\sim 7d$ 8h*	$9.8 \cdot 10^4$	64	12h 20	57
IST	$152 \times 152 \times 17 \times 3$	$5.1 \cdot 10^6$	152	3d 11h	$8.8 \cdot 10^4$	38	5h 30	60
ALOHA	$152 \times 152 \times 17 \times 3$	$5.1 \cdot 10^6$	152	$\sim 25d$ 1h*	$8.8 \cdot 10^4$	38	1d 14h 25	62

Table II: Comparison of the learning-based random variable-density Gaussian sampling optimization (Alg. 2) for different settings. n_{pars} denotes the number of parameters that were tuned. For each set of parameters, the results were averaged on 20 masks drawn at random from the distribution considered. The computations were done for 12 different sampling rates.

Algo.	Setting	n_{pars}	n_{recon}	n_{procs}	Time
KTF	$152 \times 152 \times 17 \times 3$	120	$8.6 \cdot 10^4$	38	6h 30
	$256 \times 256 \times 10 \times 2$	240	$1.05 \cdot 10^5$	64	6h 45
IST	$152 \times 152 \times 17 \times 3$	120	$8.6 \cdot 10^4$	38	3h 20
ALOHA	$152 \times 152 \times 17 \times 3$	120	$8.6 \cdot 10^4$	38	1d 8h

Coherence-based variable-density Gaussian sampling (Coherence-VD): The computation times using variable-density methods are almost negligible compared to the greedy and LB-VD running times because no reconstruction is involved. Therefore, they will not be reported.

IV. RESULTS

A. Comparison between the greedy algorithms

In this first experiment, we compare the three variations of the greedy algorithms that were previously discussed, namely the regular *greedy* algorithm 1.a, the *stochastic* greedy algorithm 1.b which takes k samples (entire lines in Fourier space at different phase encodes) uniformly at random at each iteration, and the *stochastic cycling* greedy algorithm 1.c, which takes k samples in a given frame at each iteration. We use the cardiac dataset and split the data between 3 training and 4 testing samples. We chose the number of stochastic samples to be $k = 38$, as Figure 1A highlights that the PSNR is very close for all three greedy methods. This fact can seem surprising considering that the *stochastic* and *stochastic cycling* methods use 68 times less possible phase encodes than the *greedy* Algorithm 1.a at each iteration. A similar behavior was observed for larger k , and generally, unless one uses extremely small batches of samples (e.g. 20 or less), the stochastic greedy algorithms will yield results similar to the regular *greedy* algorithm, as seen on Figure 1B. The first supplementary section discusses the effect of batch size in greater detail, and shows results on IST. Note also that ALOHA was not run in this setup due to the prohibitive runtime of the regular greedy algorithm on it.

Visually speaking, on Figure 1C, the reconstructions are as well very similar across all three algorithms and for both sampling rates, although masks slightly differ. As we are looking for an approximate maximizer, several sampling mask can satisfy this criterion. Moreover, we see that the the stochastic algorithms actually outperforms the *greedy* algorithm in the range 20–30% with KTF. This can be explained by the randomness allowing to explore a larger selection of mask configurations by helping to exit the local optima in which the greedy method could get stuck.

Overall, both stochastic greedy Algorithms 1.b and 1c yield similar PSNR and visual quality as Algorithm 1.a for a fraction of its computational cost, and we will prefer the *stochastic cycling greedy* algorithm over the *stochastic greedy*, as it has the additional benefit of keeping a fixed number of readouts per frame. In the sequel, this algorithm will use a batch of 38 samples with 3 training data of size $152 \times 152 \times 17$, unless otherwise specified.

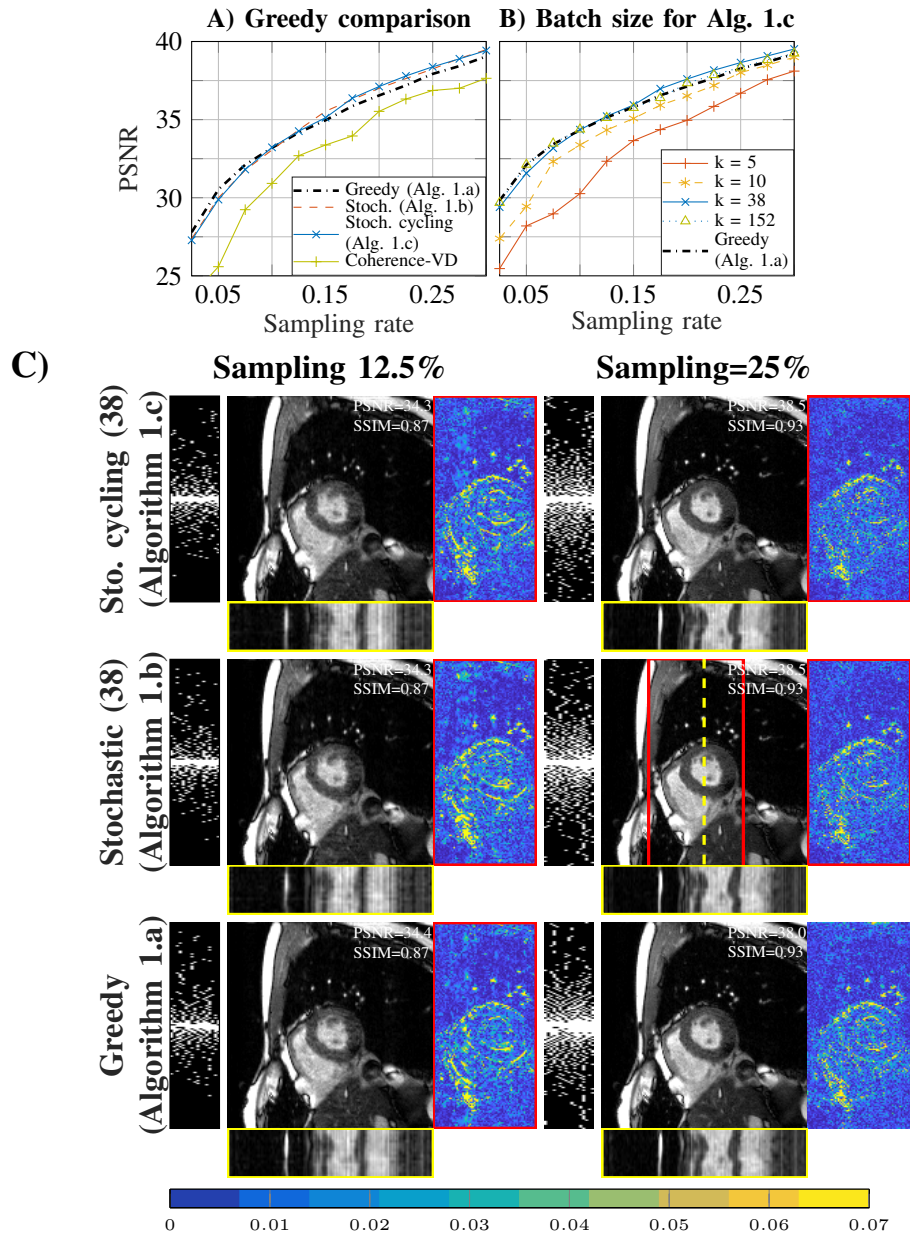


Figure 1: A) PSNR as a function of sampling rates for the three greedy algorithms considered, compared to the Coherence-VD sampling [23] for KTF.

B) PSNR as a function of the sampling rate for KTF, comparing the effect of the batch size on the quality of the reconstruction for Algorithm 1.c.

The results were averaged on 4 cardiac cine testing images of size $152 \times 152 \times 17$.

C) Comparison between the different forms of greedy algorithms using k -t FOCUSS as a reconstruction methods, for two different sampling rates (12.5% and 25%), on an image of size $152 \times 152 \times 17$. The ninth frame is displayed, and the temporal profile is taken across the vertical line shown on the top right image.

The stochastic and stochastic cycling greedy used batches of $k = 38$ elements.

B. Simulated undersampling of fully sampled Cartesian cardiac cine data

1) *Comparison to baselines:* The comparison to baselines is shown on Figures 2 and 3, where we see that the learning-based method yields masks which consistently improve the results compared to all variable-density methods used. Even though some variable-density techniques are able to provide good results for some sampling rates and algorithms, our learning-based technique is able to consistently provide improvement over this state-of-the-art. Compared to Coherence-VD, there is always at least 1 dB improvement at any sampling rate, and it can be as much as 6.7 dB at 5% sampling rate for ALOHA. Compared to *golden*, there is an improvement larger than

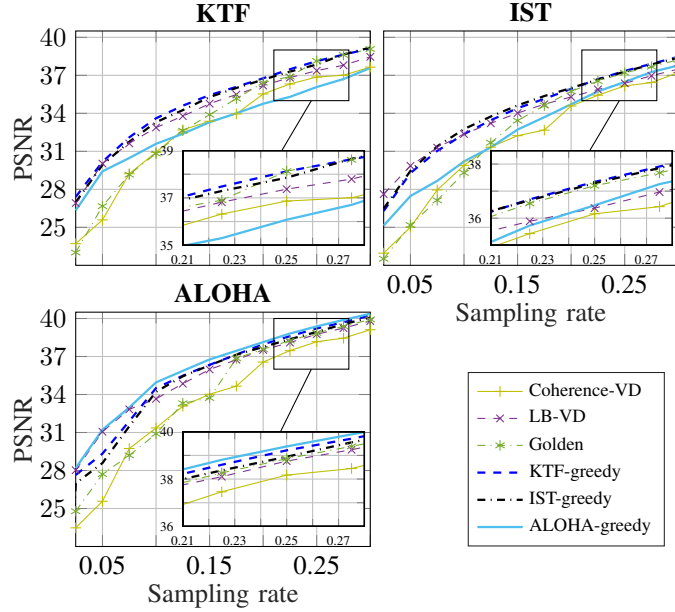


Figure 2: PSNR as a function of sampling rate for the three reconstruction algorithms considered, comparing the learning-based stochastic cycling greedy result with the coherence-based Gaussian sampling [23], Learning-based variable-density (Algorithm 2 - optimized for each reconstruction algorithm), and golden angle Cartesian sampling [28], averaged on 4 testing images of size $152 \times 152 \times 17$.

1.5 dB prior to 15% rate, and around 0.5dB after for all decoders. Figure 2 also clearly indicates that the benefits of our learning-based framework become more apparent towards higher sampling rates, where the performance improvement over LB-VD reaches up to 1 dB. Towards lower sampling rates, with much fewer degrees of freedom for mask design, the stochastic cycling greedy method and LB-VD yield similar performance as expected. As shown in Figure 3, the learning-based masks tend to conserve better the sharp contrast transition compared to the variable-density techniques.

2) *Cross-performances of reconstruction algorithms:* Referring again to Figures 2 and 3, there are several observations to be made regarding the masks resulting from the stochastic cycling greedy procedure across the decoders. First of all, the masks for KTF and IST yield performances that are very close, even when pairing them to the other decoder, where only a small drop of less than 0.5 dB is observed. Paired with the ALOHA decoder, any of these masks outperforms the baselines at the majority of the sampling rates considered. On the other hand, the mask trained with ALOHA performs suboptimally with KTF and IST decoders, yet remaining in competition with the coherence-VD mask. This is due to the fact that the ALOHA performs better with more higher frequency phase encodes, which are not preferred by KTF and IST decoders in their corresponding masks.

Additionally, we notice on Figure 3 that comparing the reconstruction algorithms with VD masks reduces the difference between each algorithm: the performance is very close in each case. Whereas considering the reconstruction algorithm jointly with a sampling pattern optimized with a model-free approach makes the performance difference much more clear: ALOHA with its corresponding mask clearly outperforms KTF and IST with their corresponding masks, which was not evident by looking only at reconstruction with VD-based masks. This is further discussed in Section 2 of the Supplementary Material, where we compare the cross-performance of LB-VD and stochastic cycling greedy masks in greater detail.

3) *Cross-performances of performance measures:* Up to this point, we used PSNR as the performance metric η , and we now compare it with the results of the stochastic cycling greedy algorithm paired with SSIM, a metric that more closely reflects perceptual similarity. For brevity, we only consider ALOHA in this section. In the case where we optimized sampling for SSIM, we noticed that unless a low-frequency initial mask is given, the reconstruction quality would mostly stagnate. This is why we chose to start the greedy algorithm with 4 low-frequency phase encodes at each frame in the SSIM case.

The reconstructions with masks optimized for PSNR and SSIM are shown on Figure 4A, where we see that the learning-based masks outperform the state-of-the-art across all sampling rates except at 2.5% in the SSIM case. The quality of the results is very close for both masks, but each tends to perform slightly better with the performance

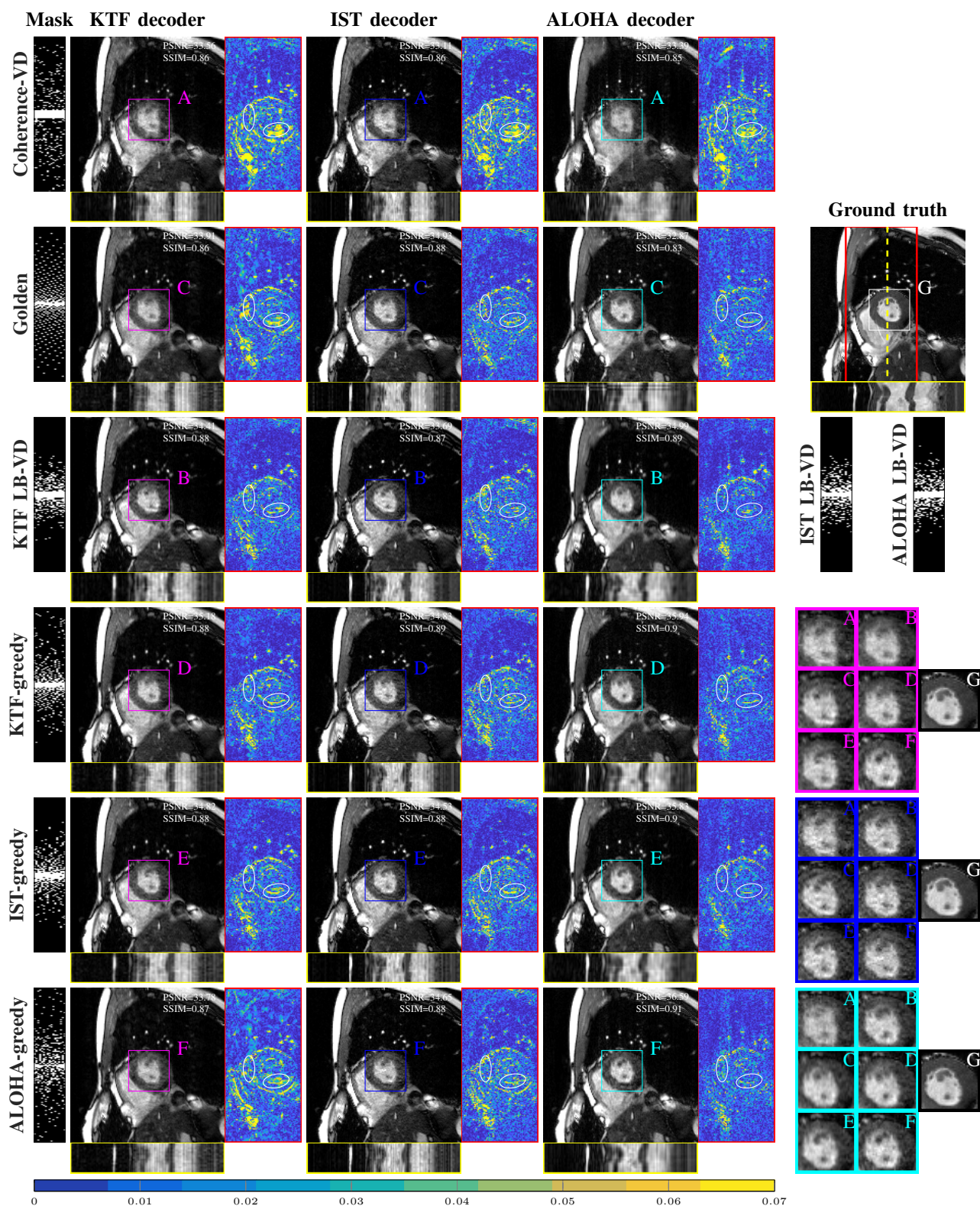


Figure 3: Comparison of the different reconstruction masks and decoders, for a sampling rate of 15% on a single sample of size $152 \times 152 \times 17$, with the ninth frame displayed. The comparison are the *Coherence-VD* sampling [23], *LB-VD* (Alg. 2 - optimized for each reconstruction algorithm), and *golden-ratio Cartesian sampling* [28], as well as the masks optimized for each reconstruction algorithm using *stochastic cycling greedy Algorithm 1.c*. Temporal profiles are taken across the dashed line shown on the ground truth, and the error maps are taken between the red lines on the ground truth, and computed with respect to a unit normalized ground truth. An additional comparison of *LB-VD* and *stochastic cycling greedy masks* is available in Figure 4 in the Supplementary Material.

metric for which it was trained. The fact that the ALOHA-SSIM result at 2.5% has a very low SSIM is due to the fact that we impose 4 phase encodes across all frames, and the resulting sampling mask at 2.5% is a low pass mask in this case.

A visual reconstruction is provided in Figure 4B we see that there is almost no difference in reconstruction quality, and that the masks remain very similar. Overall, we observe in this case that the performance metric selection does not have a dramatic effect on the quality of reconstruction, and our greedy framework is still able to produce masks that outperform state-of-the-art when optimizing SSIM instead of PSNR.

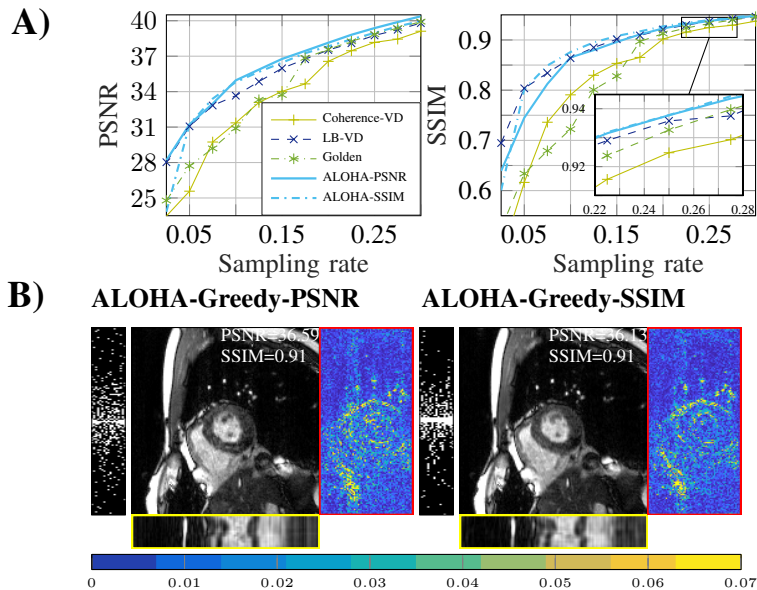


Figure 4: A) PSNR and SSIM as a function of sampling rate for ALOHA, comparing the learning-based stochastic cycling greedy masks and reconstructions optimized for PSNR and SSIM with the three baselines, averaged on 4 testing images of size $152 \times 152 \times 17$.

B) Comparison of the sampling masks optimized for PSNR and SSIM with ALOHA, at 15% sampling. The images and masks can be compared to those of Figure 3, as the settings are the same.

C. Simulated undersampling of fully sampled Cartesian cardiac cine and vocal tract data with a larger image size

In these last experiments, we considered both a cardiac dataset and a vocal dataset of sizes $256 \times 256 \times 10$. The cardiac dataset was trained on 5 samples and tested on 2, using only the first ten frames of each scan, whereas the vocal one used 2 training samples and 2 testing samples. In this setup, the k-space of the cardiac dataset tends to vary more from one sample to another than the vocal one, making the generalization of the mask more complicated. This issue would require more training samples, but imposing the stochastic cycling greedy algorithm to start with 4 central phase encoding lines on each frame was found to be sufficient to acquire the peaks in the k-space across the whole dataset. *Cardiac-greedy* refers to the stochastic cycling greedy algorithm using cardiac data, and *Vocal-greedy* is its vocal counterpart. The algorithm used a batch of size $k = 64$ at each iteration, and the results were obtained using only KTF.

The results are reported on the Figures 5 and 6, and we see that, for the both datasets, the stochastic cycling greedy approach provides superior results against state-of-the-art sampling methods across all sampling rates. It is important to note that, in this setting, our approach outperforms even more convincingly all the baselines; the LB-VD approach is outperformed by more than 2dB by the greedy approach, where it remained very competitive in the other setting. Additionally, we see that it is important for the trained mask to be paired with its anatomy to obtain the best performance.

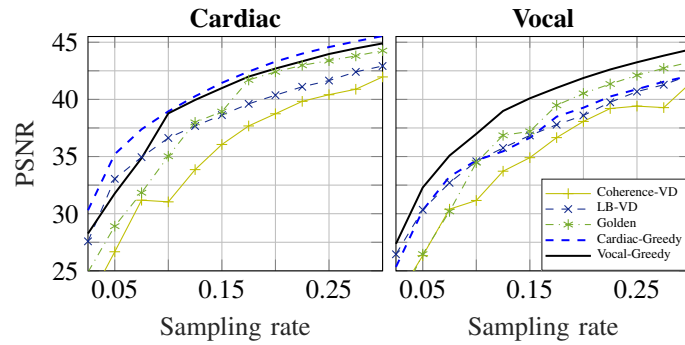


Figure 5: PSNR as a function of sampling rate for KTF, comparing the learning-based stochastic cycling greedy result with both baselines, averaged on 2 testing images for both cardiac and vocal datasets of size $256 \times 256 \times 10$.

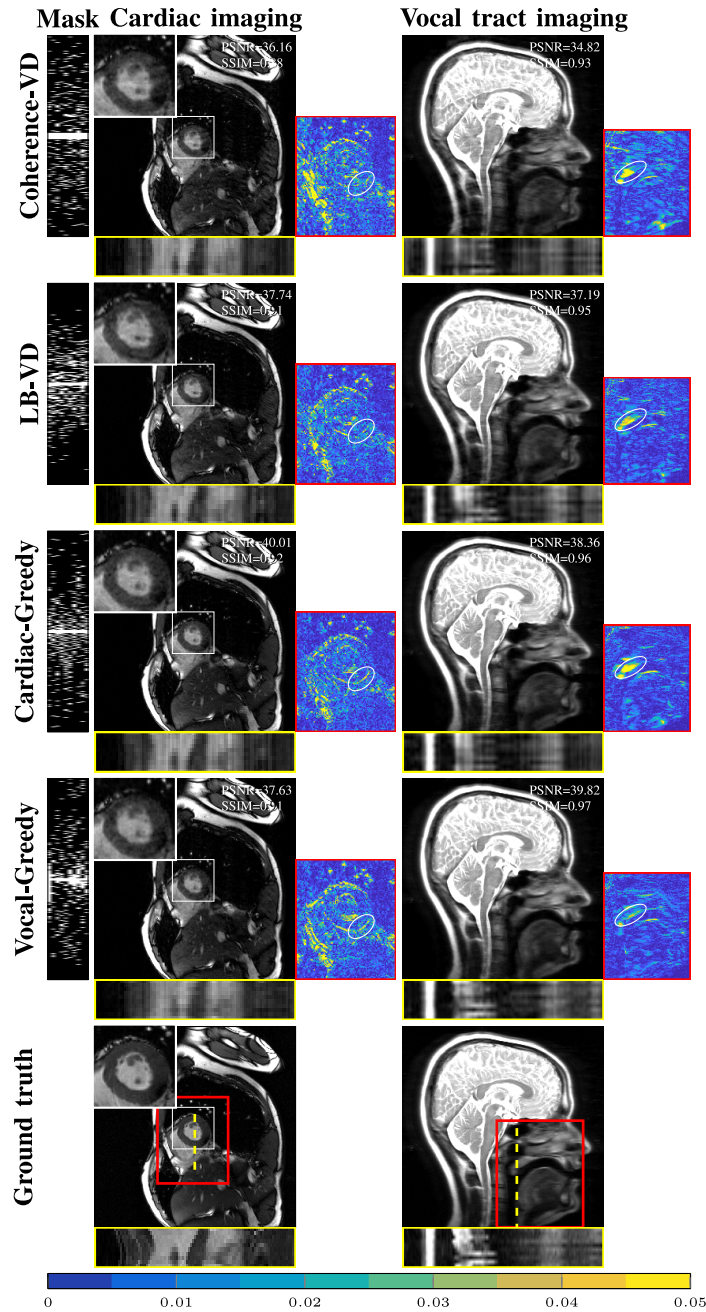


Figure 6: Reconstruction for KTF at 15% sampling for the cardiac and vocal anatomies of size $256 \times 256 \times 10$. Figures showing different frames for the vocal and cardiac images are available in Section 3 of Supplementary Material.

V. DISCUSSION

In this work, we presented a data-driven method for sampling optimization in the dMRI setting which brings considerable image quality improvements over the state-of-the-art methods. These model-based methods limit the performance of CS applied to MRI through their underlying model and are consistently outperformed by our model-free method on different in vivo datasets, across several decoders, field of views and resolutions. Our findings highlight that sampling design should not be considered in isolation from data and reconstruction algorithm, as using a mask that is not specifically optimized can considerably degrade the performance of the algorithm. We see this clearly on Figures 2 and 3, where the reconstructions using LB-VD exhibit very similar performances due to the constraints on mask design, with performances in the range of 34 – 35 dB, whereas our model-free approach yields more diverse sampling masks which in return lead to a performance increase to a 35 – 37 dB range. Moreover, our approach is able to provide masks with performance guarantees on unseen data, whereas the VD approach relies on random sampling and parameter tuning, which complicates the incorporation of compressed sensing-based methods into routine clinical MRI [41].

While the present work used relatively small datasets, the stochastic greedy method can be improved to incorporate larger datasets at a reasonable computational cost. This can be achieved by randomly selecting a batch of training samples at each iteration instead of the whole training set; moreover, the computations on different images of the dataset could also be performed in parallel in order to further parallelize the computations of the proposed stochastic greedy method.

The present work focused only on single-coil experiments for simplicity, however an extension to the multi-coil MRI [42]–[44] would be of prime importance. The main difficulty in this setting comes from the necessity to estimate coil sensitivities. A possible solution could be to initialize the stochastic greedy algorithm with a certain number of central phase encodes taken by default at the beginning which then can be used as a calibration region to estimate the coil sensitivities, in a similar fashion that was performed in experiments IV-B3 and IV-C.

We foresee various other future directions for our work. Non-Cartesian masks such as radial masks are known to be more robust to the motion, therefore it could be of high importance to investigate the potential benefits of our approach in the radial setting. On the other hand, recently emerging deep learning methods for image reconstruction are to be incorporated to our framework which would enable learning both sampling and reconstruction from data as a means of further enhancing the overall image quality performance.

VI. CONCLUSION

The stochastic greedy method proposed in this work successfully obtains optimized masks for dMRI on cardiac and vocal datasets, yielding a consistent improvement over model-based sampling methods commonly used in the Cartesian setting, such as Gaussian variable-density random sampling. Additionally, the proposed methods largely resolved the scalability issues of [35], while preserving its advantages of being intuitive, versatile, and easy to pair with any reconstruction and anatomy. Reducing the resources used in the greedy algorithm by as much as a 60 times was shown to have no negative impact on the quality of reconstruction achieved within our framework.

VII. SUPPORTING INFORMATION

1) Influence of the batch size k on the mask design

- **Figure 1** PSNR as a function of the sampling rate for KTF, comparing the effect of the batch size on the quality of the reconstruction for Algorithms 1.b (on the left) and 1.c (on the right).
- **Figure 2** Learning-based masks obtained with the *stochastic* greedy algorithm (Algorithm 1.b) for different batch sizes k using KTF as a reconstruction algorithm.
- **Figure 3** Learning-based masks obtained with the *stochastic cycling* greedy algorithm (Algorithm 1.c) for different batch sizes k using k-t FOCUSS as a reconstruction algorithm.

2) Comparison of performances between LB-VD and Stochastic cycling greedy algorithms

- **Figure 4** Extension of Figure 3, comparing LB-VD with *stochastic cycling greedy*, for a sampling rate of 15% on a single sample with the corresponding PSNR/SSIM performances.
- **Figure 5** PSNR as a function of sampling rate for the three reconstruction algorithms considered, comparing the learning-based *stochastic cycling greedy* result with the *LB-VD* (Algorithm 2 - optimized for each reconstruction algorithm).

3) Additional visualization of reconstructions for cardiac and vocal datasets

- **Figure 6** Reconstruction with KTF [6] at 15% sampling rate for the cardiac anatomy of size $256 \times 256 \times 10$. It unfolds the temporal profile of Figure 6.
- **Figure 7** Reconstruction with KTF [6] at 15% sampling rate for the vocal anatomy of size $256 \times 256 \times 10$. It unfolds the temporal profile of Figure 6.

4) Noisy setup

- **Figure 8 A)** PSNR as a function of sampling rate for both reconstruction algorithms considered, comparing the learning-based *stochastic cycling greedy* result with the three baselines, averaged on 4 noisy testing images.
- B) Reconstructed denoised version from the noisy ground truth on the first line, at 15% sampling.

ACKNOWLEDGMENT

This work has received funding from the European Research Council (ERC) under the European Union’s Horizon 2020 research and innovation program (grant agreement n° 725594 - time-data) and from Hasler Foundation Program: Cyber Human Systems (project number 16066).

REFERENCES

- [1] M. Saeed, T. A. Van, R. Krug, S. W. Hetts, and M. W. Wilson, “Cardiac MR imaging: current status and future direction,” *Cardiovascular diagnosis and therapy*, vol. 5, no. 4, p. 290, 2015.
- [2] E. J. Candes, J. K. Romberg, and T. Tao, “Stable signal recovery from incomplete and inaccurate measurements,” *Communications on pure and applied mathematics*, vol. 59, no. 8, pp. 1207–1223, 2006.
- [3] D. L. Donoho, “Compressed sensing,” *IEEE transactions on Information Theory*, vol. 52, no. 4, pp. 1289–1306, 2006.
- [4] M. Lustig, J. M. Santos, D. L. Donoho, and J. M. Pauly, “ $k - t$ SPARSE: High frame rate dynamic MRI exploiting spatio-temporal sparsity,” in *Proc. of the 13th Annual Meeting of ISMRM, Seattle*, vol. 2420, 2006.
- [5] U. Gamper, P. Boesiger, and S. Kozerke, “Compressed sensing in dynamic MRI,” *Magnetic Resonance in Medicine*, vol. 59, no. 2, pp. 365–373, 2008.
- [6] H. Jung, K. Sung, K. S. Nayak, E. Y. Kim, and J. C. Ye, “k-t FOCUSS: A general compressed sensing framework for high resolution dynamic MRI,” *Magn. Reson. Med.*, vol. 61, no. 1, pp. 103–116, 2009.
- [7] R. Otazo, D. Kim, L. Axel, and D. K. Sodickson, “Combination of compressed sensing and parallel imaging for highly accelerated first-pass cardiac perfusion MRI,” *Magnetic Resonance in Medicine*, vol. 64, no. 3, pp. 767–776, 2010.
- [8] M. Usman, C. Prieto, T. Schaeffter, and P. Batchelor, “k-t group sparse: A method for accelerating dynamic MRI,” *Magnetic Resonance in Medicine*, vol. 66, no. 4, pp. 1163–1176, 2011.
- [9] A. Majumdar, R. K. Ward, and T. Aboulnasr, “Compressed sensing based real-time dynamic MRI reconstruction,” *IEEE Transactions on Medical Imaging*, vol. 31, no. 12, pp. 2253–2266, 2012.
- [10] B. Zhao, J. P. Haldar, A. G. Christodoulou, and Z.-P. Liang, “Image reconstruction from highly undersampled (k, t) -space data with joint partial separability and sparsity constraints,” *IEEE Transactions on Medical Imaging*, vol. 31, no. 9, pp. 1809–1820, 2012.
- [11] R. Otazo, L. Feng, H. Chandarana, T. Block, L. Axel, and D. K. Sodickson, “Combination of compressed sensing and parallel imaging for highly-accelerated dynamic MRI,” in *Biomed. Imaging (ISBI), 2012 9th IEEE International Symposium on*. IEEE, 2012, pp. 980–983.
- [12] L. Feng, R. Grimm, K. T. Block, H. Chandarana, S. Kim, J. Xu, L. Axel, D. K. Sodickson, and R. Otazo, “Golden-angle radial sparse parallel MRI: Combination of compressed sensing, parallel imaging, and golden-angle radial sampling for fast and flexible dynamic volumetric MRI,” *Magnetic Resonance in Medicine*, vol. 72, no. 3, pp. 707–717, 2014.
- [13] B. Trémouh  ac, N. Dikaios, D. Atkinson, and S. R. Arridge, “Dynamic MR image reconstruction—separation from undersampled (k, t) -space via low-rank plus sparse prior,” *IEEE Transactions on Medical Imaging*, vol. 33, no. 8, pp. 1689–1701, 2014.
- [14] R. Otazo, E. Cand  es, and D. K. Sodickson, “Low-rank plus sparse matrix decomposition for accelerated dynamic MRI with separation of background and dynamic components,” *Magnetic Resonance in Medicine*, vol. 73, no. 3, pp. 1125–1136, 2015.
- [15] J. Schlemper, J. Caballero, J. V. Hajnal, A. N. Price, and D. Rueckert, “A deep cascade of convolutional neural networks for dynamic MR image reconstruction,” *IEEE Transactions on Medical Imaging*, vol. 37, no. 2, pp. 491–503, 2018.
- [16] S. G. Lingala and M. Jacob, “Blind compressive sensing dynamic MRI,” *IEEE transactions on medical imaging*, vol. 32, no. 6, pp. 1132–1145, 2013.
- [17] Y. Wang and L. Ying, “Compressed sensing dynamic cardiac cine MRI using learned spatiotemporal dictionary,” *IEEE transactions on Biomedical Engineering*, vol. 61, no. 4, pp. 1109–1120, 2014.
- [18] J. Caballero, A. N. Price, D. Rueckert, and J. V. Hajnal, “Dictionary learning and time sparsity for dynamic MR data reconstruction,” *IEEE Transactions on Medical Imaging*, vol. 33, no. 4, pp. 979–994, 2014.
- [19] S. G. Lingala, Y. Hu, E. DiBella, and M. Jacob, “Accelerated dynamic MRI exploiting sparsity and low-rank structure: k-t SLR,” *IEEE Transactions on Medical Imaging*, vol. 30, no. 5, pp. 1042–1054, 2011.
- [20] H. Yoon, K. S. Kim, D. Kim, Y. Bresler, and J. C. Ye, “Motion adaptive patch-based low-rank approach for compressed sensing cardiac cine MRI,” *IEEE Transactions on Medical Imaging*, vol. 33, no. 11, pp. 2069–2085, 2014.
- [21] K. H. Jin, D. Lee, and J. C. Ye, “A general framework for compressed sensing and parallel MRI using annihilating filter based low-rank Hankel matrix,” *IEEE Transactions on Computational Imaging*, vol. 2, no. 4, pp. 480–495, 2016.

- [22] E. J. Candès, J. Romberg, and T. Tao, “Robust uncertainty principles: Exact signal reconstruction from highly incomplete frequency information,” *IEEE Trans. on Inf. Theory*, vol. 52, no. 2, pp. 489–509, 2006.
- [23] M. Lustig, D. Donoho, and J. M. Pauly, “Sparse MRI: The application of compressed sensing for rapid MR imaging,” *Magnetic Resonance in Medicine*, vol. 58, no. 6, pp. 1182–1195, 2007.
- [24] H. Jung, J. C. Ye, and E. Y. Kim, “Improved k-t BLAST and k-t SENSE using FOCUSS,” *Physics in medicine and biology*, vol. 52, no. 11, p. 3201, 2007.
- [25] D. Kim, H. A. Dyvorne, R. Otazo, L. Feng, D. K. Sodickson, and V. S. Lee, “Accelerated phase-contrast cine MRI using k-t SPARSE-SENSE,” *Magnetic Resonance in Medicine*, vol. 67, no. 4, pp. 1054–1064, 2012.
- [26] L. Weizman, Y. C. Eldar, and D. Ben Bashat, “Compressed sensing for longitudinal MRI: An adaptive-weighted approach,” *Medical physics*, vol. 42, no. 9, pp. 5195–5208, 2015.
- [27] R. Ahmad, H. Xue, S. Giri, Y. Ding, J. Craft, and O. P. Simonetti, “Variable density incoherent spatiotemporal acquisition (VISTA) for highly accelerated cardiac MRI,” *Magnetic Resonance in Medicine*, vol. 74, no. 5, pp. 1266–1278, 2015.
- [28] S. Li, Y. Zhu, Y. Xie, and S. Gao, “Dynamic magnetic resonance imaging method based on golden-ratio cartesian sampling and compressed sensing,” *PLoS one*, vol. 13, no. 1, p. e0191569, 2018.
- [29] M. Seeger, H. Nickisch, R. Pohmann, and B. Schölkopf, “Optimization of k-space trajectories for compressed sensing by bayesian experimental design,” *Magn. Reson. Med.*, vol. 63, no. 1, pp. 116–126, 2010.
- [30] F. Knoll, C. Clason, C. Diwoy, and R. Stollberger, “Adapted random sampling patterns for accelerated MRI,” *Magnetic resonance materials in physics, biology and medicine*, vol. 24, no. 1, pp. 43–50, 2011.
- [31] S. Ravishankar and Y. Bresler, “Adaptive sampling design for compressed sensing MRI,” in *Engineering in Medicine and Biology Society, EMBC, 2011 Annual International Conference of the IEEE*. IEEE, 2011, pp. 3751–3755.
- [32] D.-d. Liu, D. Liang, X. Liu, and Y.-t. Zhang, “Under-sampling trajectory design for compressed sensing MRI,” in *Engineering in Medicine and Biology Society (EMBC), 2012 Annual International Conference of the IEEE*. IEEE, 2012, pp. 73–76.
- [33] Y. Zhang, B. S. Peterson, G. Ji, and Z. Dong, “Energy preserved sampling for compressed sensing MRI,” *Computational and mathematical methods in medicine*, vol. 2014, 2014.
- [34] J. Vellagoundar and R. R. Machireddy, “A robust adaptive sampling method for faster acquisition of MR images,” *Magnetic resonance imaging*, vol. 33, no. 5, pp. 635–643, 2015.
- [35] B. Gözcü, R. K. Mahabadi, Y.-H. Li, E. Ilıcak, T. Cukur, J. Scarlett, and V. Cevher, “Learning-based compressive MRI,” *IEEE transactions on medical imaging*, vol. 37, no. 6, pp. 1394–1406, 2018.
- [36] S. Ravishankar and Y. Bresler, “MR image reconstruction from highly undersampled k-space data by dictionary learning,” *IEEE Transactions on Medical Imaging*, vol. 30, no. 5, pp. 1028–1041, 2011.
- [37] L. Feng, L. Axel, H. Chandarana, K. T. Block, D. K. Sodickson, and R. Otazo, “XD-GRASP: Golden-angle radial MRI with reconstruction of extra motion-state dimensions using compressed sensing,” *Magnetic Resonance in Medicine*, vol. 75, no. 2, pp. 775–788, 2016.
- [38] Z. Wang, A. C. Bovik, H. R. Sheikh, and E. P. Simoncelli, “Image quality assessment: from error visibility to structural similarity,” *IEEE transactions on image processing*, vol. 13, no. 4, pp. 600–612, 2004.
- [39] D. O. Walsh, A. F. Gmitro, and M. W. Marcellin, “Adaptive reconstruction of phased array mr imagery,” *Magnetic Resonance in Medicine*, vol. 43, no. 5, pp. 682–690, 2000.
- [40] M. A. Griswold, D. Walsh, R. M. Heidemann, A. Haase, and P. M. Jakob, “The use of an adaptive reconstruction for array coil sensitivity mapping and intensity normalization,” in *International Society for Magnetic Resonance in Medicine (ISMRM), Proceedings of the 10th Scientific Meeting*, 2002, p. 2410.
- [41] L. Axel and R. Otazo, “Accelerated MRI for the assessment of cardiac function,” *The British journal of radiology*, vol. 89, no. 1063, p. 20150655, 2016.
- [42] K. P. Pruessmann, M. Weiger, M. B. Scheidegger, P. Boesiger *et al.*, “SENSE: sensitivity encoding for fast MRI,” *Magnetic Resonance in Medicine*, vol. 42, no. 5, pp. 952–962, 1999.
- [43] M. A. Griswold, P. M. Jakob, R. M. Heidemann, M. Nittka, V. Jellus, J. Wang, B. Kiefer, and A. Haase, “Generalized autocalibrating partially parallel acquisitions (GRAPPA),” *Magnetic Resonance in Medicine*, vol. 47, no. 6, pp. 1202–1210, 2002.
- [44] M. Blaimer, F. Breuer, M. Mueller, R. M. Heidemann, M. A. Griswold, and P. M. Jakob, “SMASH, SENSE, PILS, GRAPPA: how to choose the optimal method,” *Topics in Magnetic Resonance Imaging*, vol. 15, no. 4, pp. 223–236, 2004.
- [45] T. Sanchez, B. Gözcü, R. B. van Heeswijk, E. Ilıcak, T. Çukur *et al.*, “Scalable learning-based sampling optimization for compressive dynamic mri,” *arXiv preprint*, vol. 1902.00386, 2019.
- [46] M. Maggioni, G. Boracchi, A. Foi, and K. Egiazarian, “Video denoising, deblocking, and enhancement through separable 4-D nonlocal spatiotemporal transforms,” *IEEE Transactions on image processing*, vol. 21, no. 9, pp. 3952–3966, 2012.

APPENDIX A
INFLUENCE OF THE BATCH SIZE k ON THE MASK DESIGN

In this appendix, we further discuss the tuning of the batch size used already seen in section IV-A. We compare more batch sizes than in section IV-A and show the masks resulting from different stages of sampling. We ran the stochastic greedy algorithms with different batch sizes in the same setting of section IV-A and report on Figure 7 the PSNR of the reconstructions for the *stochastic* and the *stochastic cycling* greedy algorithms respectively. We only considered KTF for brevity again. As mentioned in section IV-A, unless the batch size is extremely small (less than 1.5% of all phase encoding lines at each greedy iteration), the results suggest that the masks obtained with Algorithms 1.b and 1.c yield satisfactory reconstruction quality, i.e. the same quality as the standard greedy algorithm or even an increased quality.

The Figures 8 and 9 show the different masks obtained for the batch sizes considered and several observations can be made. First of all, as expected, taking a batch size of 1 yields a totally random mask, and taking a batch size of 5 yields a mask that is more centered around the low frequencies than the one with $k = 1$ but is still spread out. Then, as the batch size increases, resulting masks seem to converge to very similar designs.

While this detailed analysis was performed using exclusively KTF, we observed similar behaviors for the other reconstruction algorithms. This suggests that, overall, the effect of the batch size might be independent from the reconstruction algorithm. In general, we observe that, using a batch size that is a reasonable fraction of the size of the data, the algorithm will exhibit similar performance as the original greedy algorithm.

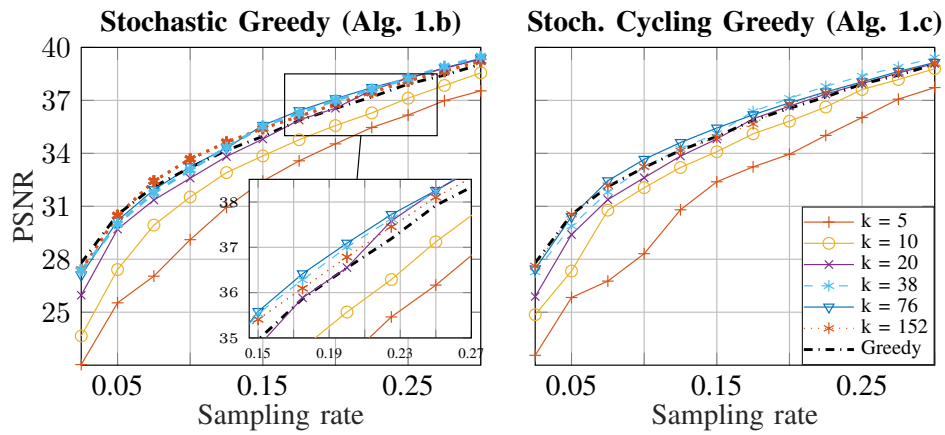


Figure 7: PSNR as a function of the sampling rate for KTF, comparing the effect of the batch size on the quality of the reconstruction for Algorithms 1.b (on the left) and 1.c (on the right). The result is averaged on 4 testing images of size $152 \times 152 \times 17$. Here, Greedy corresponds to Algorithm 1.a, and is shown for comparison.

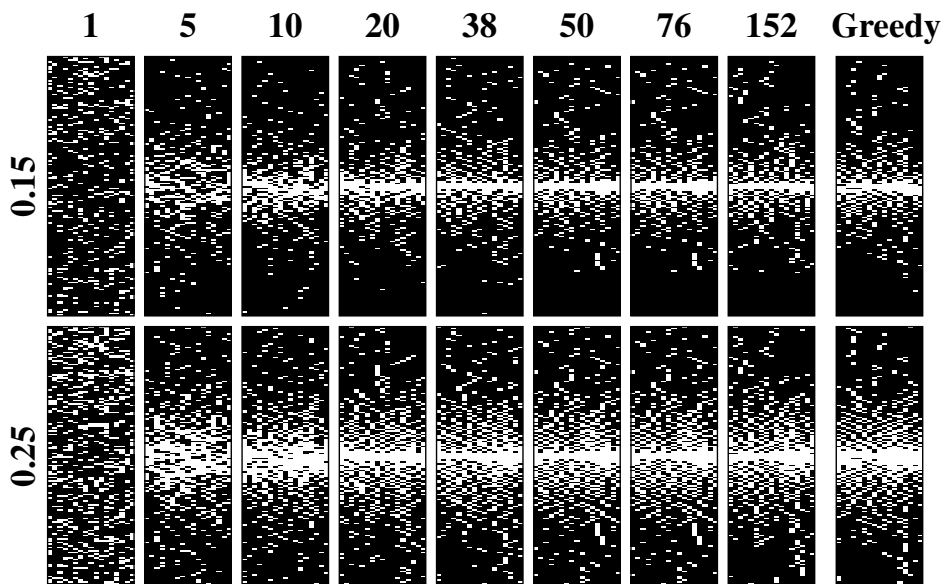


Figure 8: Learning-based masks obtained with the *stochastic greedy* algorithm (Algorithm 1.b) for different batch sizes k using KTF as a reconstruction algorithm, shown in the title of each column, for 15% (top) and 25% (bottom) sampling rate. The optimization used data of size $152 \times 152 \times 17$ with 3 training samples, with a total of 2584 possible phase encoding lines for the masks to pick from. Here, *Greedy* corresponds to Algorithm 1.a.

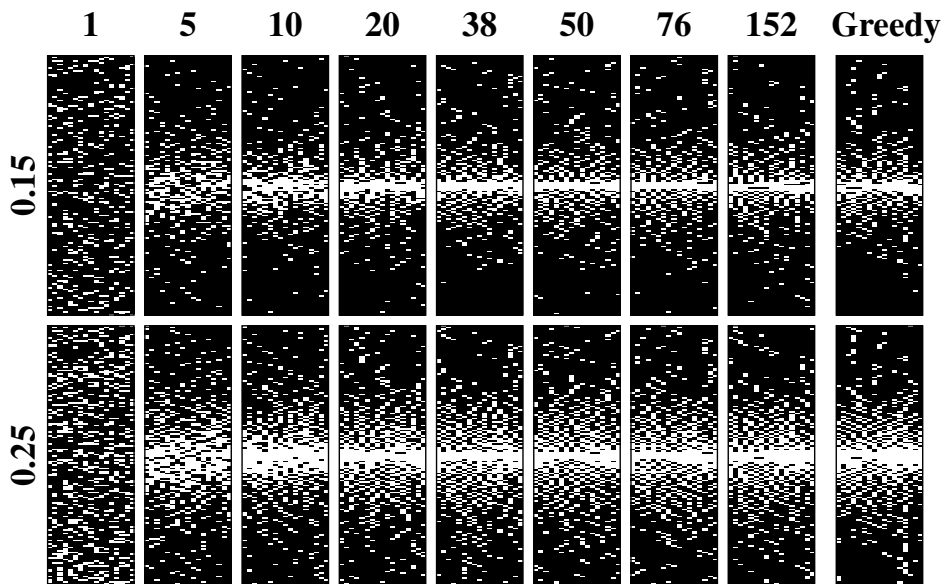


Figure 9: Learning-based masks obtained with the *stochastic cycling greedy* algorithm (Algorithm 1.c) for different batch sizes k using KTF as a reconstruction algorithm, shown in the title of each column, for 15% (top) and 25% (bottom) sampling rate. The optimization used data of size $152 \times 152 \times 17$ with 3 training samples, with a total of 2584 possible phase encoding lines for the masks to pick from. Here, *Greedy* corresponds to Algorithm 1.a.

APPENDIX B

COMPARISON OF PERFORMANCES BETWEEN LB-VD AND STOCHASTIC CYCLING GREEDY ALGORITHMS

In this appendix, we compare in greater detail the performances and the cross-performances of masks trained with LB-VD and Stochastic cycling greedy algorithms. On Figure 10, we compare these two algorithms when the trained mask is paired with its reconstruction algorithm, for a different frame than the one of Figure 3. On this Figure, we globally see that stochastic cycling greedy masks are able to provide a reconstruction which overall has lower errors than the one using LB-VD, which is especially noticeable on the ALOHA reconstruction, on the edge of the left ventricle.

The result of Figure 11 extends what was shown on Figure 2 by considering the cross-performance plots for LB-VD. A first observation is that the cross-performance of LB-VD masks does not show much variation across different algorithms: all three performances are always closely related, and usually are not able to match the performance from the greedy mask paired with the reconstruction algorithm for which it was trained. The reason for this similarity comes from the design of the LB-VD method: due to the few parameters that it has, the best parameters do not change significantly across different decoders, which results in similar masks in all cases, as shown on Figure 10, where all LB-VD masks are similar.

On the other hand, the model-free stochastic cycling greedy approach results in widely different masks that considerably improve the reconstruction quality of the reconstruction algorithm for which it was trained.

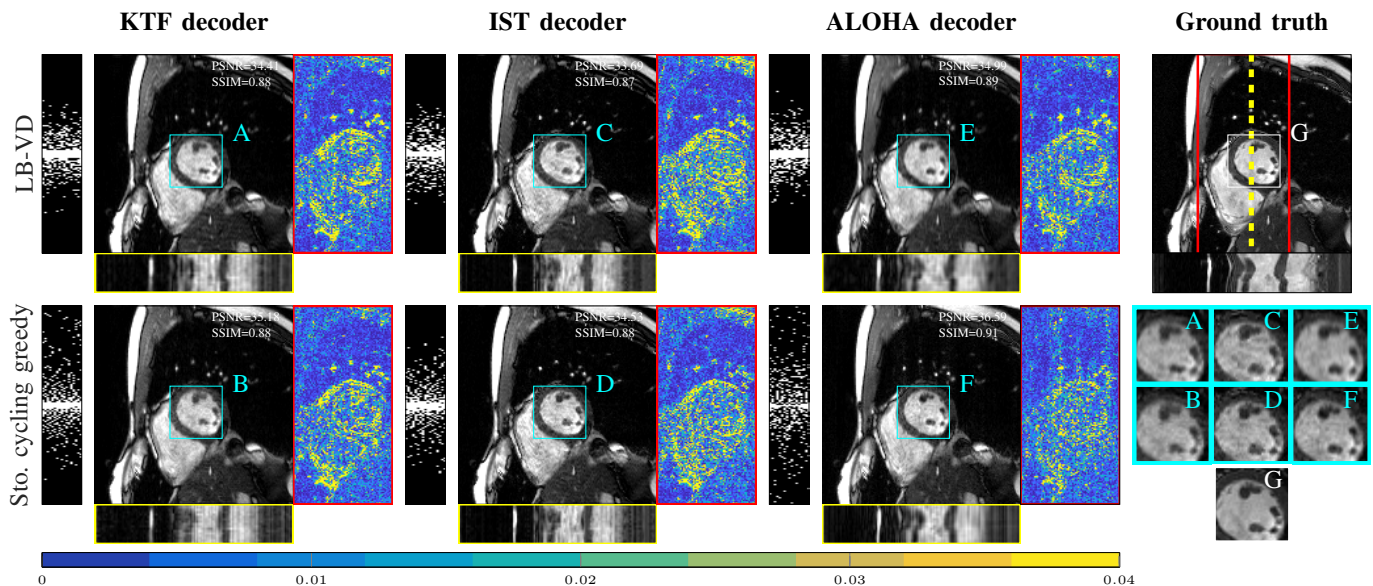


Figure 10: Extension of Figure 3, comparing LB-VD with stochastic cycling greedy, for a sampling rate of 15% on a single sample with the corresponding PSNR/SSIM performances. These are images of size $152 \times 152 \times 17$. The fourteenth frame is displayed, and the temporal profile is taken across the vertical line shown on the ground truth, and is displayed below each image.

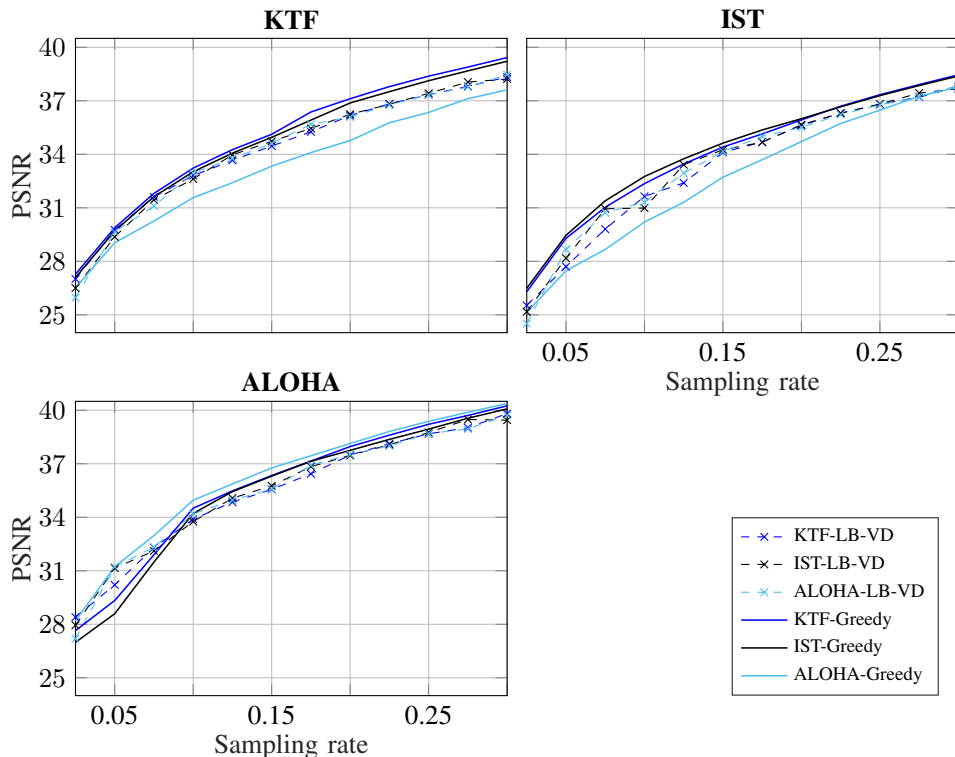


Figure 11: PSNR as a function of sampling rate for the three reconstruction algorithms considered, comparing the learning-based stochastic cycling greedy result with the LB-VD (Algorithm 2 - optimized for each reconstruction algorithm), averaged on 4 testing images of size $152 \times 152 \times 17$. The setting is the same as in Figure 2.

APPENDIX C

ADDITIONAL VISUALIZATION OF RECONSTRUCTIONS FOR CARDIAC AND VOCAL DATASETS

The present appendix provides further results for Section IV-C. We show in Figures 12 and 13 reconstructions at different frames which provide clearer visual information about the quality of reconstruction than the temporal profiles used in the article. Due to space restrictions, it was however not possible to include these along with the main numerical results.

For these images, the PSNR and SSIM are computed with respect to each individual frame, showing the quality of the reconstruction in a detailed fashion. Generally, as previously observed, the mask trained for a specific anatomy will most faithfully capture the sharp contrast transitions in the dynamic regions of the images, which is clearly visible on the error maps. For the vocal tract images, we notice once again in the error maps that while all learning-based methods perform relatively well, the mask obtained by our stochastic greedy algorithm using the vocal tract training dataset produces the least sharpness loss compared to the other masks.

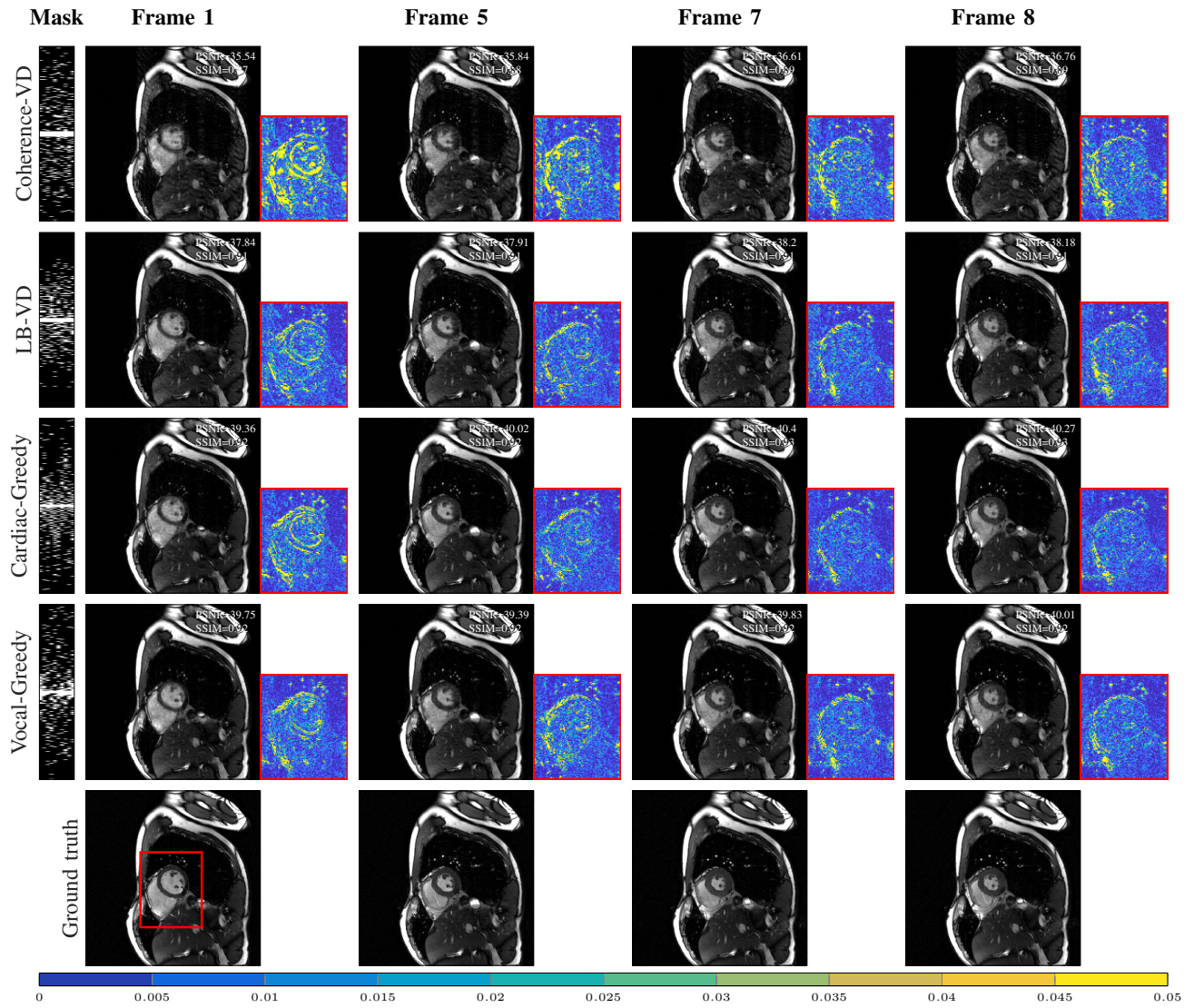


Figure 12: Reconstruction with KTF [6] at 15% sampling rate for the cardiac anatomy of size $256 \times 256 \times 10$. It unfolds the temporal profile of Figure 6. The PSNR and SSIM displayed are computed for each image. The ground truth is added at the end of each column for comparison.

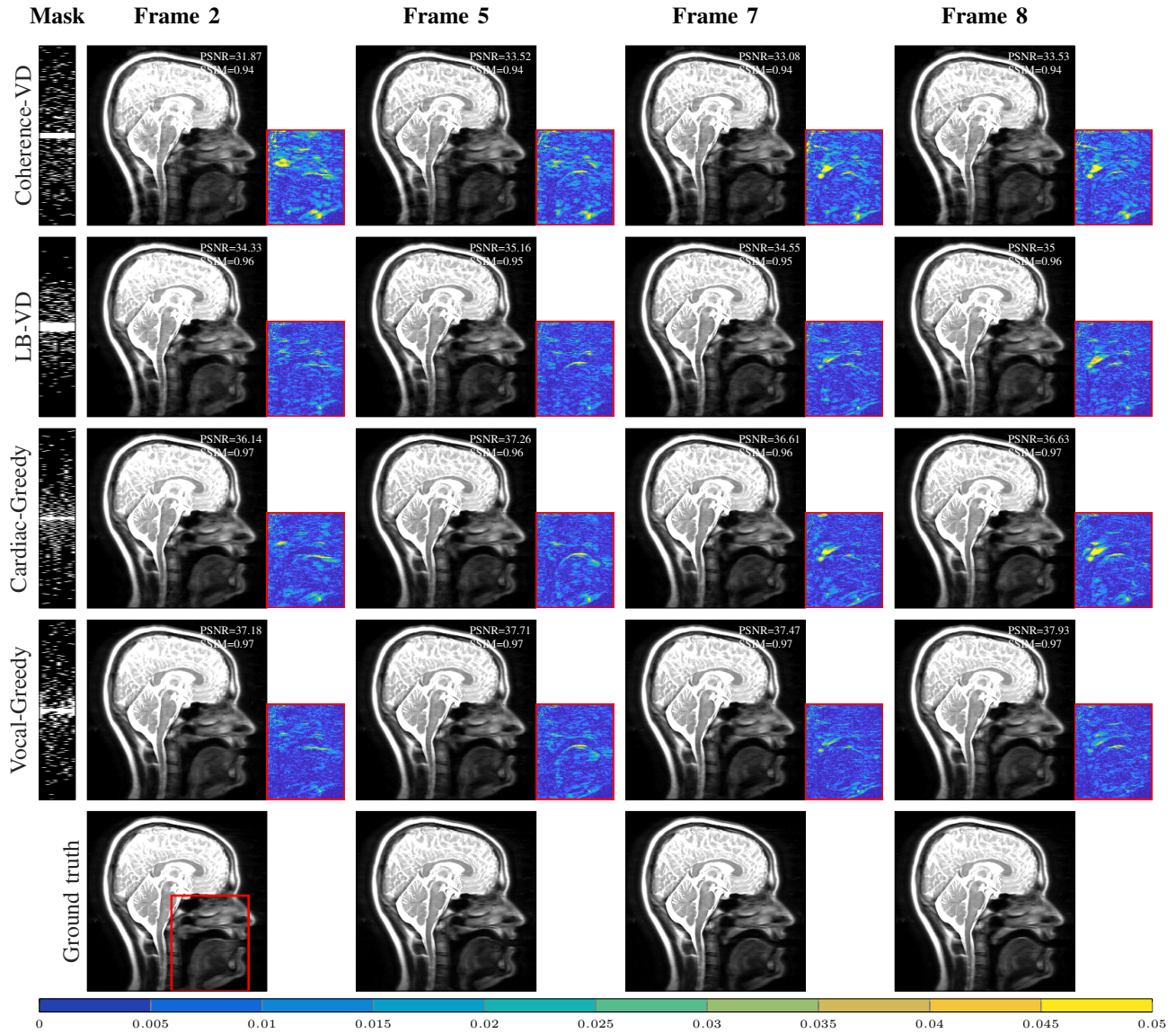


Figure 13: Reconstruction with KTF [6] at 15% sampling rate for the vocal anatomy of size $256 \times 256 \times 10$. It unfolds the temporal profile of Figure 6. The PSNR and SSIM displayed are computed for each image. The ground truth is added at the end of each line for comparison.

APPENDIX D
NOISY SETUP

A. *Theory*

In the noisy case, we again consider the same setup as in [35], where we do not have access to the exact training samples $\mathbf{x}_1, \dots, \mathbf{x}_m$, but only to a noisy version of those

$$\mathbf{z}_j = \mathbf{x}_j + \mathbf{v}_j, \quad j = 1, \dots, m \quad (7)$$

where \mathbf{v}_j is the noise in the samples, and we have the relation $\mathbf{w}_j = \mathbf{\Psi}\mathbf{v}_j$. Again, as we want to learn the true underlying signal and not the noisy one, we use a denoiser $\xi(\mathbf{z}_j) = \mathbf{x}_j + \tilde{\mathbf{v}}_j$ that reduces the noise level, i.e. $\mathbb{E}[\|\tilde{\mathbf{v}}_j\|] \leq \mathbb{E}[\|\mathbf{v}_j\|]$, and the empirical risk minimization formulation is then adapted to

$$\hat{\Omega} = \operatorname{argmax}_{\Omega \in \mathcal{A}} \frac{1}{m} \sum_{j=1}^m \eta_{\Omega}(\mathbf{x}_j + \tilde{\mathbf{v}}_j, \hat{\mathbf{x}}(\mathbf{P}_{\Omega}\mathbf{\Psi}(\mathbf{x}_j + \mathbf{v}_j))). \quad (8)$$

Using the noisy training signal $\mathbf{b} = \mathbf{P}_{\Omega}\mathbf{\Psi}\mathbf{x} + \mathbf{w}$ allows the algorithm to choose samples that will enable it to denoise the testing signal, which also has noisy samples. The generalization bound of Proposition 2 of [35] remains valid in the present case.

B. *Results*

In order to test the robustness of our framework to noise, we artificially added bivariate circularly symmetry complex random Gaussian noise to the normalized complex images, with a standard deviation $\sigma = 0.05$ for both the real and imaginary components. We then tested to see whether the greedy framework is able to adapt to the level of noise by prescribing a different sampling pattern than in the previous experiments.

We chose to use V-BM4D [46] as denoiser with its default suggested mode using Wiener filtering and low-complexity profile, and provided the algorithm the standard deviation of the noise as the denoising parameter. The comparison between the fully sampled denoised images and the original ones yields an average PSNR of 24.95 dB across the whole dataset. Due to the fact that none of the reconstruction algorithms that we used have a denoising parameter incorporated, we simply apply the V-BM4D respectively to the real and the imaginary parts of the result of the reconstruction. The results that we obtain are presented on the Figures 14A and 14B.

It is interesting to notice on Figure 14B that the learning-based framework outperforms the baselines that are not learning-based by a larger margin than in the noiseless case, and this is again especially true at low sampling rates. In this case however, the difference between the greedy and LB-VD methods is much smaller, and this might be explained by the fact that noise corrupts the high frequency samples, and thus the masks concentrate more around low-frequencies, leaving less room for designs that largely differ.

Also, notice that the inadequacy of coherence-based sampling is highlighted in this case, as very little temporal information is captured in the reconstruction with both decoders. Also, for both decoders, there is a clear improvement on the preservation of the temporal profile when using learning-based masks compared to the baselines; the improvement of the ALOHA-greedy mask of around 3dB also shows how well our framework is able to adapt to this noisy situation, whereas Coherence-VD yields results of unacceptable quality.

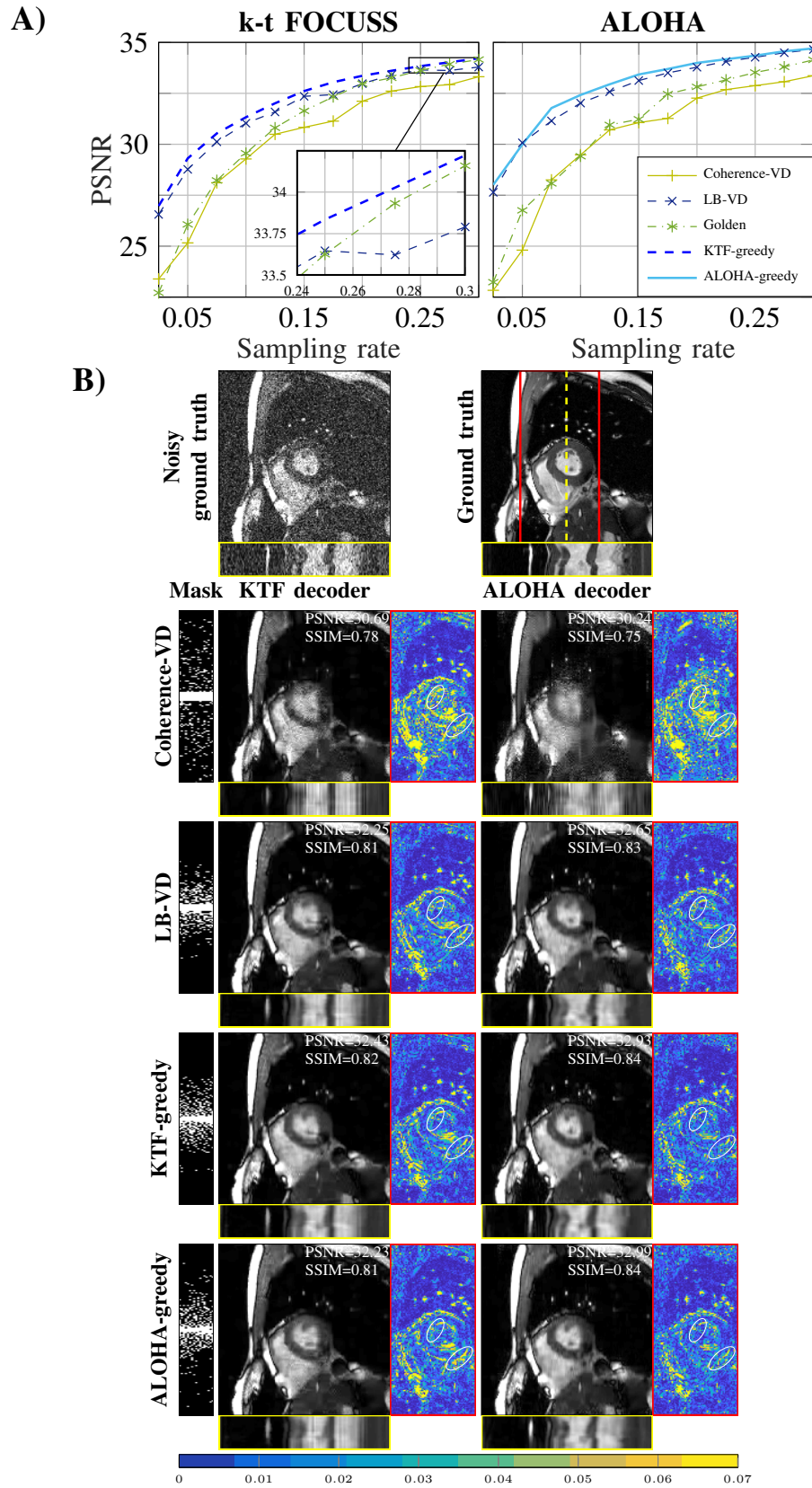


Figure 14: A) PSNR as a function of sampling rate for both reconstruction algorithms considered, comparing the learning-based stochastic cycling greedy result with the three baselines, averaged on 4 noisy testing images of size $152 \times 152 \times 17$. The PSNR is computed between the denoised reconstructed image and the original (not noisy) ground truth.

B) Reconstructed denoised version from the noisy ground truth on the first line, at 15% sampling. The PSNR is computed with respect to the original ground truth on the top right.